

Article

Highly Efficient Photo-Degradation of Gaseous Organic Pollutants Catalyzed by Diatomite-Supported Titanium Dioxide

Xuefei Liu ¹, Yugan He ¹, Beibei Yang ¹, Qi Yan ² and Junjiao Yang ^{1,2,*}

¹ College of Chemistry, Beijing University of Chemical Technology, Beijing 100029, China; liuxf0116@163.com (X.L.); buct201093037@icloud.com (Y.H.); yangbeibei8896@163.com (B.Y.)

² Analysis and Test Center of Beijing University of Chemical Technology, Beijing University of Chemical Technology, Beijing 100029, China; yanqi0604@mail.buct.edu.cn

* Correspondence: yangjj@mail.buct.edu.cn

Received: 15 February 2020; Accepted: 27 March 2020; Published: 1 April 2020



Abstract: Volatile organic compounds (VOCs) are the most harmful contaminants that have been identified, most of which are gaseous organic pollutants. In this study, TiO₂@diatomite catalysts with various loading amounts of TiO₂ were fabricated using a facile solvothermal method with anhydrous ethanol as a solvent for the removal of VOCs. X-ray diffraction analysis revealed that TiO₂ has an anatase phase and the introduction of diatomite has no negative effect. The catalysts were characterized using scanning electron microscopy and transmittance electron microscopy techniques. The results indicate that after introducing diatomite, TiO₂ nanoparticles are mostly square-like and intact, and are uniformly immobilized in the diatomite. Finally, their photocatalytic performance was investigated using liquid ultraviolet spectrometry and gas chromatography-mass spectrometry. Among the catalysts tested, 0.35TiO₂@diatomite (with a mass ratio of TiO₂ to diatomite of 0.35) exhibited higher photocatalytic activity than the other samples, i.e., pure TiO₂ and diatomite, and could effectively remove acetone and benzene, demonstrating its potential market application and practical significance.

Keywords: gaseous organic pollutants; titanium dioxide; diatomite; photocatalysis; volatile organic compounds

1. Introduction

Volatile organic compounds (VOCs) are dominant components of indoor air pollutants. Mainly originating from decorative materials, such as carpets, paints, wallpapers, or PVC, they are also emitted or generated during human activities such as cooking or smoking tobacco [1–4]. Their harm to human health can thus not be ignored. The main problems resulting from VOCs have been reported by numerous researchers, such as Dai et al., who reported the characteristics and inhalation health risks of VOCs in newly renovated homes in Shanghai, China, and concluded that the concentrations of some VOCs present a mean cancer risk above the acceptable level [5]. Data on the respiratory effects of indoor air pollution among the elderly have been scarce. Therefore, Bentayeb et al. reported the effects of indoor air pollution on the respiratory health of the elderly, and found certain links between a variety of diseases, including respiratory diseases, and indoor air pollution [6]. In addition, Ye et al. estimated the acute cardiorespiratory effects of ambient volatile organic compounds, and their findings further support a link between incomplete combustion and cardiovascular health, as well as a link between atmospheric oxidation products and respiratory health [7]. The above studies have commonly concluded that VOCs are extremely harmful to human health. In addition, according to a survey conducted by the World Health Organization (WHO), the number of premature deaths

caused by indoor pollution globally has reached 4 million per year, and the number of deaths from indoor pollution in China is as high as 111,000, or approximately 304 per day. In addition, a 2002 report published by the WHO clearly listed indoor air pollution as one of the top causes of harm to human health [8].

Therefore, it is extremely important to study technologies regarding the removal of VOCs, and VOC removal has recently been considered by numerous researchers [9–17]. The materials used in such studies are variable, and mainly include TiO₂, ZnO, SnO₂, CdS, WO₃, and numerous other metal oxides. Among them, TiO₂ has been widely applied owing to its low-cost, non-toxicity, and high photo-catalytic activity. For instance, Šuligoj et al. reported the use of TiO₂-SiO₂ films from organic-free colloidal TiO₂ anatase nanoparticles as a photocatalyst for the removal of VOCs from air indoors [18]. In addition, Weon et al. studied an active {001} facet-exposed TiO₂ nanotube photocatalyst filter for the removal of VOCs [19]. Haghghatmamaghani, Haghghat, and Lee studied the performance of various types of commercial TiO₂ in the photocatalytic degradation of a mixture of indoor air pollutants, and adopted various alcohols, ketones, aromatics, and alkanes as the target pollutants [20].

Numerous other studies have been conducted on VOC removal using TiO₂ [21–27], and have made significant contributions to the photocatalytic degradation of such compounds. However, most of these studies have reported the use of pure TiO₂ for achieving the photo-catalytic degradation of gaseous organic pollutants. The aggregation of pure TiO₂ often limits its practical application. In addition, pure nanomaterials have their own defects, and it is therefore difficult to apply them to interior decorative materials. To solve this problem, numerous researchers are looking for a carrier for the loading of TiO₂, including porous carbon materials, Metal-Organic Frameworks, a synthetic molecular sieve, activated carbon, and many other types of artificial materials [28–31]. Not only can such materials prevent the aggregation of TiO₂, they can also improve its photodegradability.

However, the above materials must be manufactured for carrier use, and a certain cost is accrued during their synthesis. Therefore, in terms of energy efficiency, it would be better to apply natural materials, such as diatomite, which is one of the most important natural materials on Earth. With rich reserves, diatomite has abundant advantages, including non-toxicity, a stable and porous structure, strong surface adsorption, and a high heat resistance. The specific metal compounds of the material and their content are shown in Table 1 [32]. The main component is silicon dioxide, the surface of which has abundant hydroxyl and silanol groups, in which the silicon element on the surface can be bonded to TiO₂ with synergistic degradation of the gaseous organic pollutants [33–35]. In addition, Niu et al. prepared a novel diatomite-supported MnCeOx composite (MnCeOx/diatomite) characterized based on its activation of persulfate for the degradation of organic pollutants [36]. He, Luo, and Yu synthesized microdisk-like g-C₃N₄/diatomite composites utilized for the removal of methylene blue (MB) from MB/MO or MB/RhB mixed dyes [37]. Numerous other studies in this area have also been conducted [38–41]. The present study focuses on the removal of organic pollutants, the results of which will provide an exciting reference in the area of pollutant degradation.

Table 1. Chemical analyses of diatomite [32].

| Composition% | SiO ₂ | Al ₂ O ₃ | Fe ₂ O ₃ | K ₂ O | CaO | MgO | Na ₂ O | TiO ₂ | Other |
|--------------|------------------|--------------------------------|--------------------------------|------------------|------|------|-------------------|------------------|-------|
| Diatomite | 86.82 | 3.21 | 1.60 | 0.56 | 0.46 | 0.43 | 0.25 | 0.15 | 6.52 |

Thus far, TiO₂ supported by diatomite has not been utilized in the degradation of gaseous organic pollutants. Herein, we report the successful application of well-designed TiO₂@diatomite as a photo-catalytic agent for the removal of gaseous organic pollutants. In addition, diatomite was selected as a carrier, and diatomite loaded with different ratios of TiO₂ was used as a catalyst for the degradation of VOCs at room temperature under UV-Vis illumination. This catalyst is inexpensive and easy to prepare, and is thus a promising application for use in the field of interior decoration.

2. Results and Discussion

2.1. XRD Analysis

Figure 1 shows the XRD patterns of the as-prepared catalysts. Both TiO_2 and XTiO_2 @diatomite show the coexistence of an anatase phase with no additional peak, implying that no impurity appears in TiO_2 when TiO_2 is supported on diatomite. As indicated in Figure 1, the intensity of the peak at 25.27° decreases with an increase in the amount of diatomite. The diffraction peaks at 25.27° , 37.82° , 47.94° , 53.79° , 54.96° , 62.65° , 70.22° , and 75.08° correspond to the crystal faces (101), (004), (200), (105), (211), (204), (220), and (215) of anatase TiO_2 , respectively [42–44]. The peaks at 21.8° and 36.5° are attributed to the SiO_2 features in diatomite [44]. The reflection peak of diatomite becomes relatively low compared with that of TiO_2 , and the pure diatomite peak is not too weak, as shown in Figure 2 below. Therefore, the introduction of diatomite cannot affect the crystal structure of the catalyst. This result is consistent with the scanning electron microscopy (SEM) and transmittance electron microscopy (TEM) characterizations.

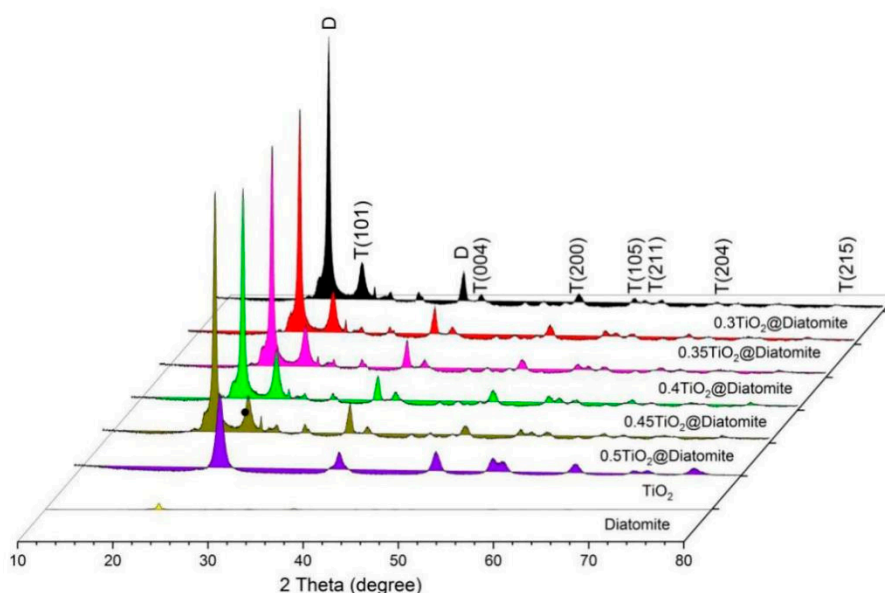


Figure 1. XRD patterns of TiO_2 , diatomite, and XTiO_2 @diatomite.

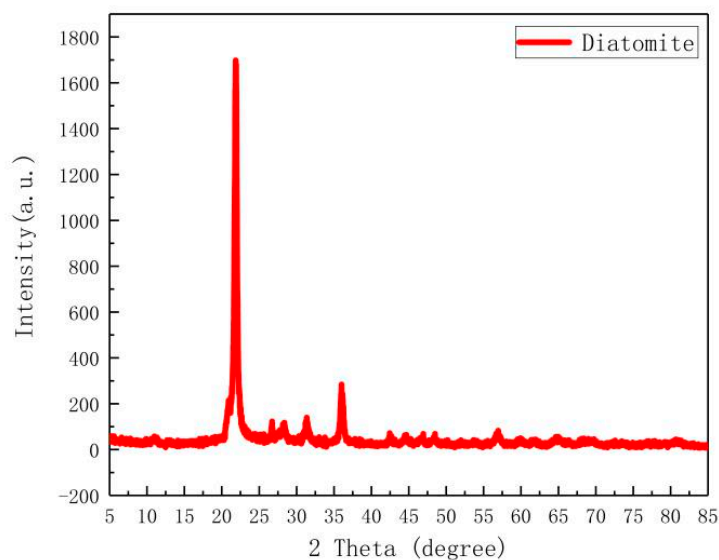


Figure 2. X-ray diffraction patterns (XRD) patterns of pure diatomite.

2.2. SEM and TEM Investigations

SEM, TEM, and high-resolution transmission electron microscopy (HRTEM) images of the catalysts are shown in Figure 3. As can be seen from Figure 3(A1,A2) in the figure, diatomite without the loading of TiO₂ nanoparticles looks like a sunflower with a smooth surface and numerous pores. The SEM images of pure TiO₂ displayed in Figure 3(B1,B2) indicate that the TiO₂ nanoparticles are square-like and approximately 10–15 nm in size, corresponding to the results of the TEM images (Figure 3(E1–E8)). As shown in Figure 3(C1–C6), the TiO₂ nanoparticles of 0.35TiO₂@diatomite are not only uniformly loaded on the surface of the diatomite, but also adhered to the pores. This indicates that TiO₂ can be firmly and evenly loaded on the surface of the diatomite. Figure 3(C1–C6) also show that the size of the TiO₂ nanoparticles loaded on the surface of the diatomite is approximately 10–15 nm, which is congruent with the TEM results shown in Figure 3(E1–E8). In addition, the other load catalysts shown in Figure 3(D1–D6) were also analyzed. As indicated in D1 and D2, the load of 0.30TiO₂@diatomite is quite small, and the surface of the diatomite is thus not completely filled with TiO₂, as opposed to 0.40TiO₂@diatomite (Figure 3(D3,D4)), 0.45TiO₂@diatomite (Figure 3(D5,D6)), and 0.50TiO₂@diatomite (Figure 3(D7,D8)). For the latter, as the load mass increases, the degree of aggregation increases significantly, and the aggregation of 0.50TiO₂@diatomite thus becomes the most serious. There is no doubt that aggregation will cause a reduction in the photocatalytic efficiency. However, the 0.35TiO₂@diatomite load mass was moderate and evenly distributed across the diatomite surface. Therefore, the catalyst of 0.35TiO₂@diatomite may perform better than other catalysts in terms of the photocatalytic efficiency for the following two reasons: First, the proportion of TiO₂ is full on the surface of the diatomite. Second, TiO₂ is evenly distributed and relatively less clustered. In addition, as shown in Figure 3(E2), the lattice distance of TiO₂ is approximately 0.35 nm, corresponding to the (101) plane of anatase TiO₂. As clearly shown above, the size of the TiO₂ nanoparticles loaded on the diatomite is nearly the same as that of pure TiO₂, indicating that the introduction of diatomite has almost no influence on the size and morphology of the TiO₂. From the HRTEM images shown in Figure 3(E1–E4), it can be clearly seen that the specific shape of TiO₂ is square-like.

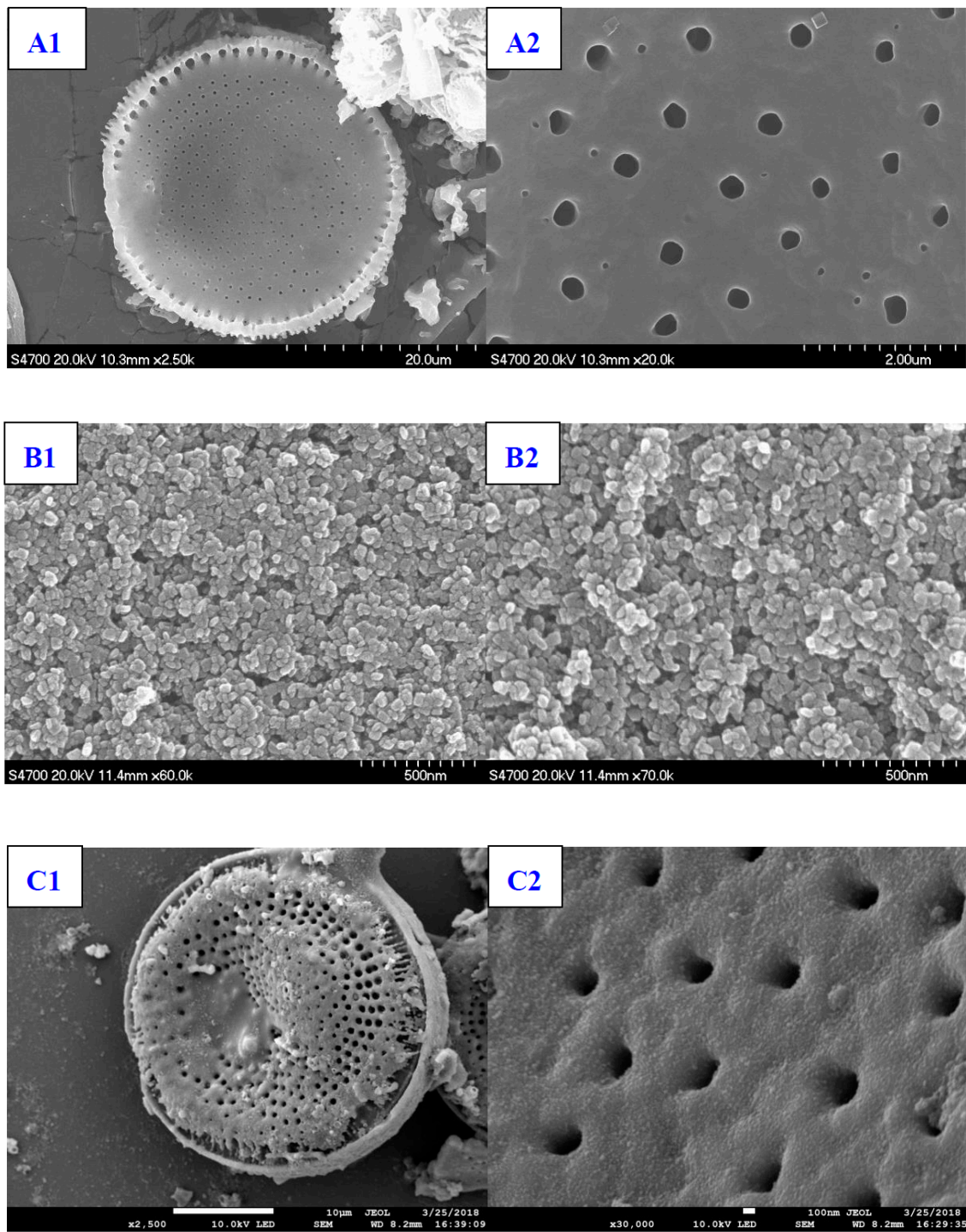


Figure 3. Cont.

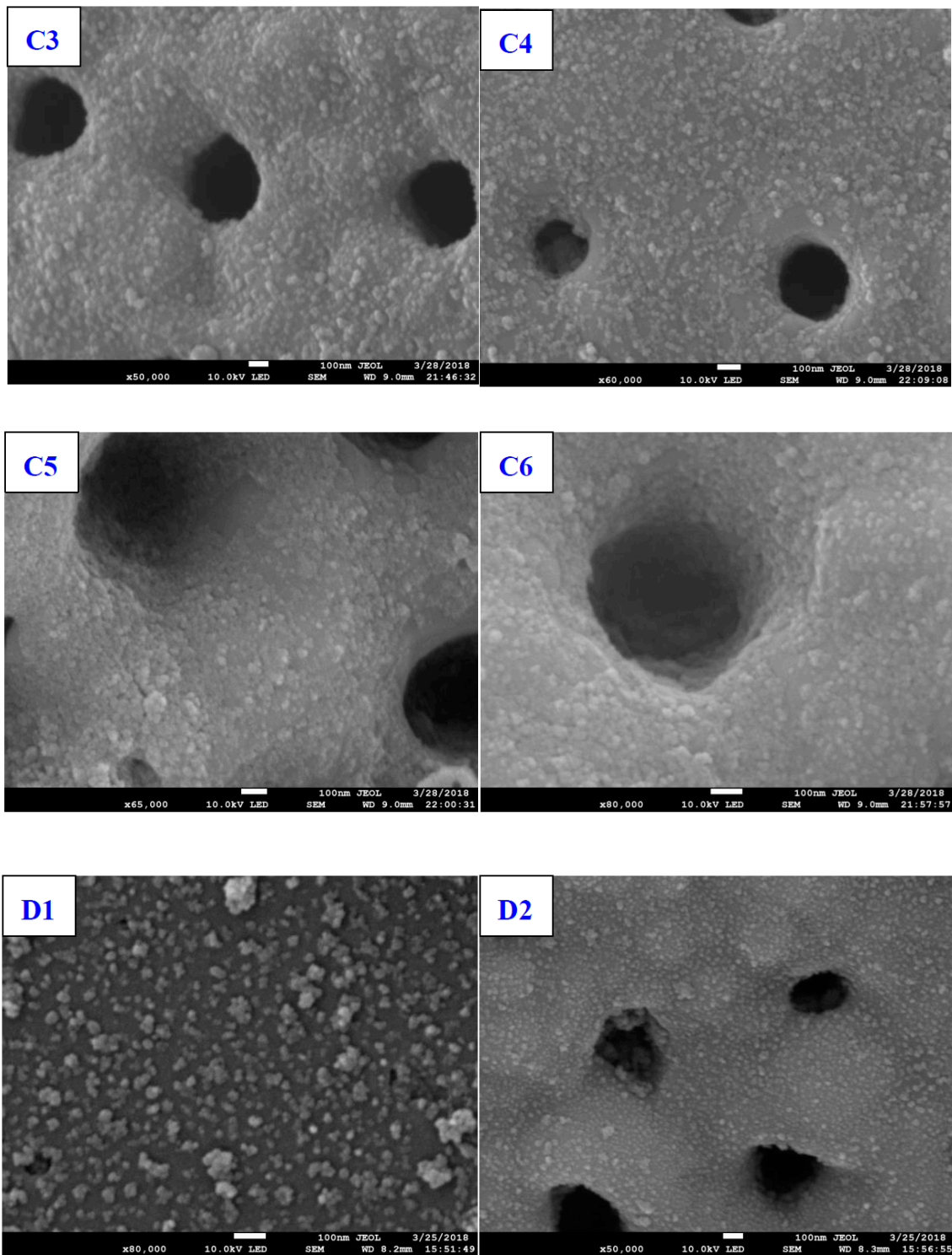


Figure 3. Cont.

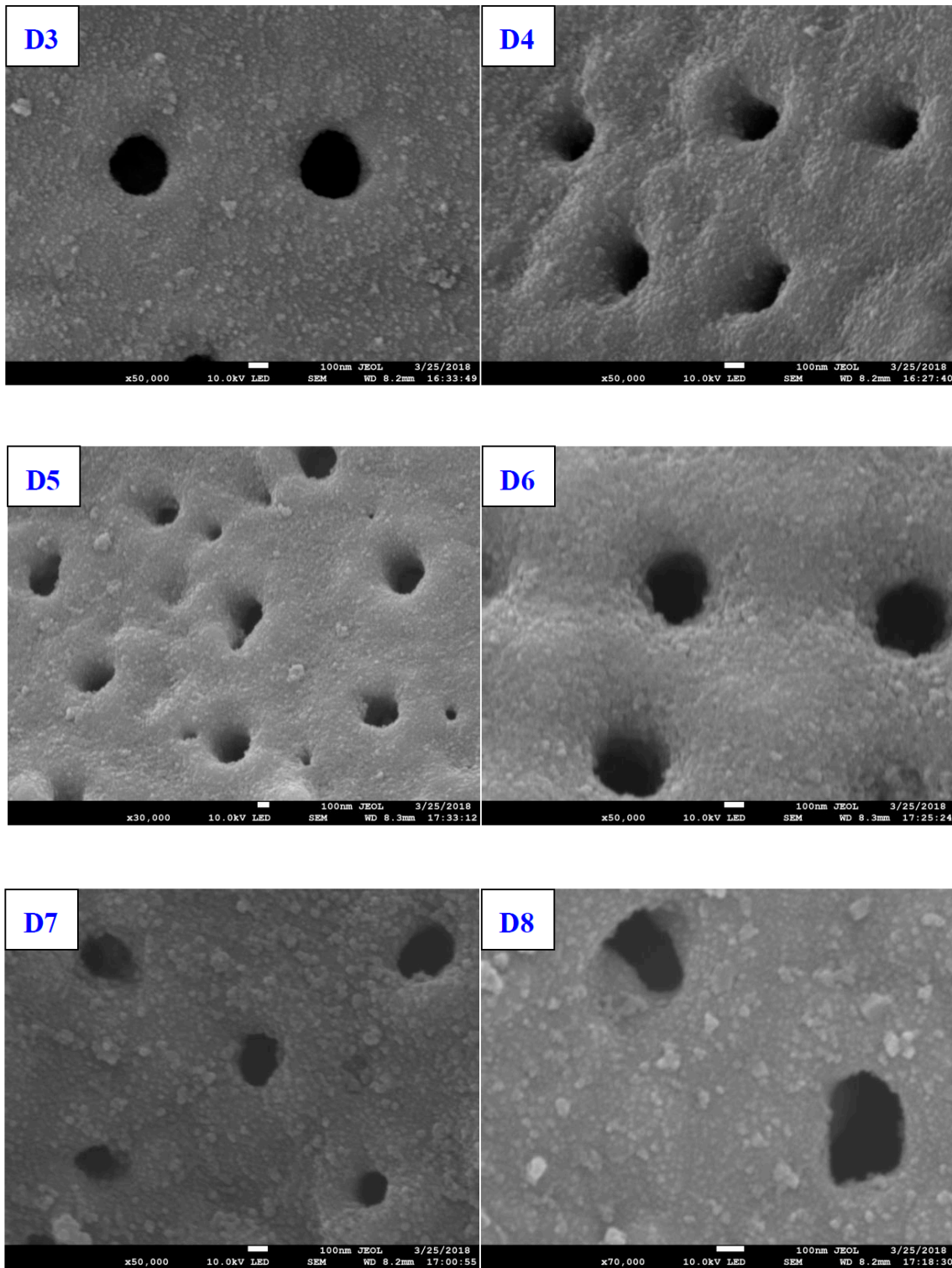


Figure 3. Cont.

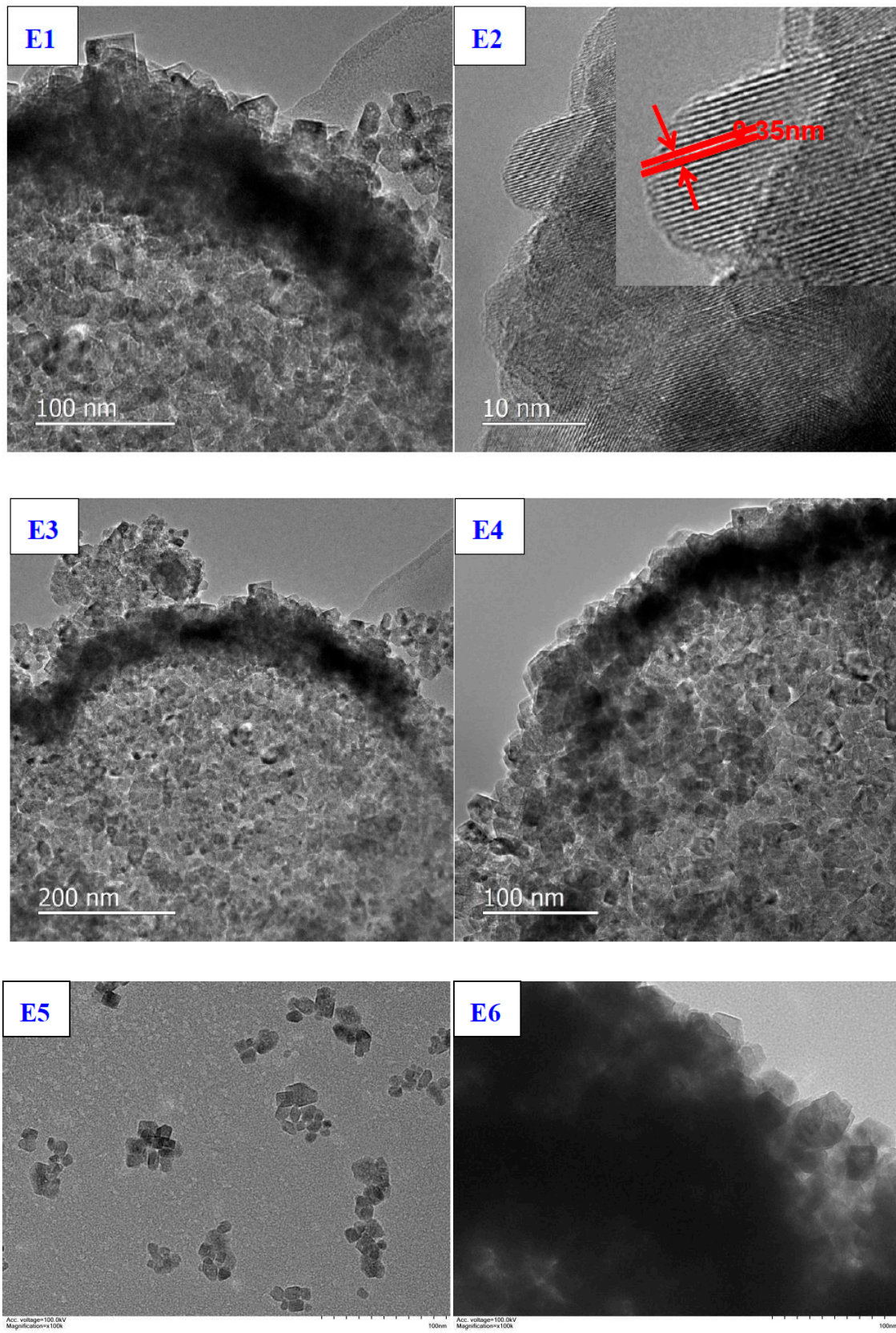


Figure 3. Cont.

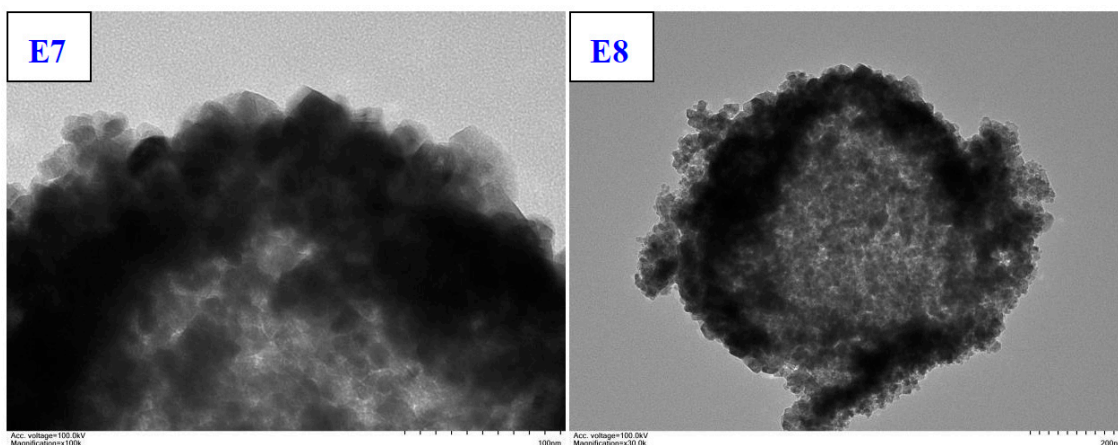


Figure 3. Scanning electron microscopy (SEM) images with different magnifications of (A1,A2) diatomite, (B1,B2) TiO_2 , (C1–C6) 0.35TiO_2 @diatomite, (D1,D2) 0.30TiO_2 @diatomite, (D3,D4) 0.40TiO_2 @diatomite, (D5,D6) 0.45TiO_2 @diatomite, and (D7,D8) 0.50TiO_2 @diatomite. (E1–E4) High-resolution transmission electron microscopy (HRTEM) images of 0.35TiO_2 @diatomite and (E5–E8) transmittance electron microscopy (TEM) images of 0.35TiO_2 @diatomite.

2.3. UV-Vis Diffuse Reflectance Spectra

As shown in Figure 4, the UV-vis diffuse reflectance spectra of the catalysts were measured to study the optical properties of the samples [45]. Clearly, for pure TiO_2 , there is no absorption at above 400 nm. However, the absorption intensity at approximately 400 nm is stronger for XTiO_2 @diatomite than for pure TiO_2 and diatomite, and the absorption (at above 400 nm) of 0.35TiO_2 @diatomite is the strongest among the XTiO_2 @diatomites considered. It can also be seen that the catalyst of TiO_2 @diatomite shows a slight red shift, suggesting that the catalyst of TiO_2 @diatomite can be excited by the visible light and thus an increase in the photocatalytic activity of the catalyst.

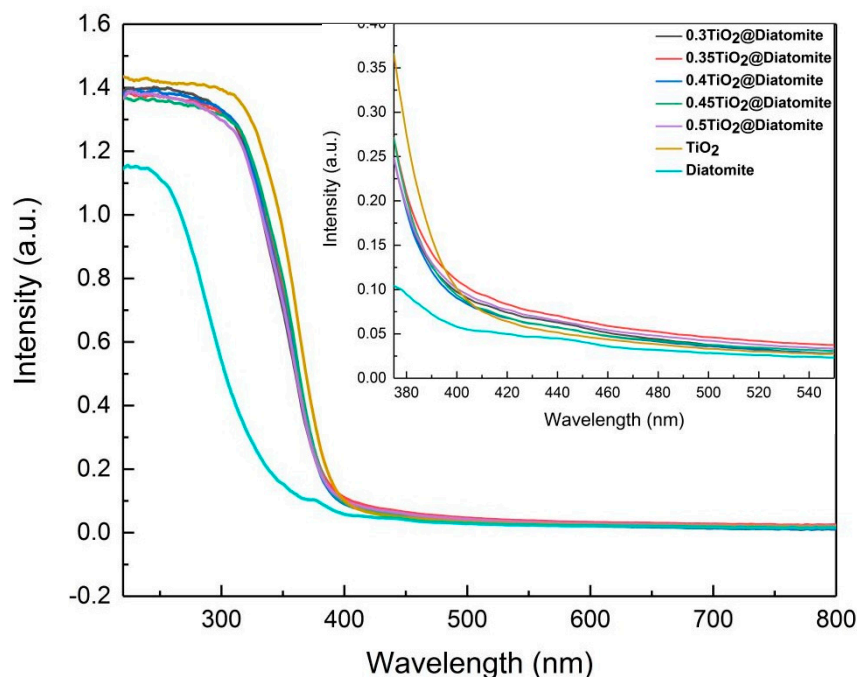


Figure 4. UV-visible diffuse reflectance adsorption spectra of the catalysts.

It can be seen from Figure 4 that pure XTiO_2 @diatomite achieves absorption at 200–400 nm, although, according to previous studies [46], pure SiO_2 has no absorption at 200–400 nm. Therefore,

the composite formed through a combination of the two with Si-O-Ti, which shows a red shift, may be attributed to the formation of this chemical bond, which reduces the energy and causes a slight red shift.

2.4. BET Analysis

The specific surface area and pore size distribution of the different catalysts were analyzed based on the nitrogen adsorption and desorption. The results are summarized in Table 2. The pure TiO₂ nanoparticles have the largest specific surface area of approximately 115.74 m²g⁻¹. However, the specific surface area and pore volume of the pure diatomite are quite small, and thus the diatomite contributes less to the specific surface area of the XTiO₂@diatomites. In other words, the specific surface areas of the catalysts were not related to the TiO₂ loadings. Therefore, the specific surface area and pore volume of the catalysts contribute little to their catalytic activity. As can be seen from Figure 5, the pure TiO₂ exhibits type-IV adsorption curves with hysteresis loops between the H1 and H2 types; the diatomite shows IUPAC type-II isotherms, indicating the presence of micropores in the diatomite [47]; and the TiO₂@diatomite composites display type-IV isotherms with an overlap of the H2 and H3 hysteresis loops, which is related to the deposition of TiO₂ nanoparticles on the surface of the diatomite.

Table 2. Surface and structural characterization of the catalysts.

| Sample | BET Specific Surface Area (m ² /g) | Pore Volume (cm ³ /g) | Average Pore Size (nm) |
|---------------------------------|---|----------------------------------|------------------------|
| Diatomite | 0.3202 | 0.002 | - |
| Pure TiO ₂ | 115.7 | 0.257 | 8.8 |
| 0.3TiO ₂ @diatomite | 20.6 | 0.044 | 8.5 |
| 0.35TiO ₂ @diatomite | 19.6 | 0.051 | 10.3 |
| 0.4TiO ₂ @diatomite | 22.3 | 0.058 | 10.5 |
| 0.45TiO ₂ @diatomite | 21.7 | 0.056 | 10.4 |
| 0.5TiO ₂ @diatomite | 21.0 | 0.050 | 9.5 |

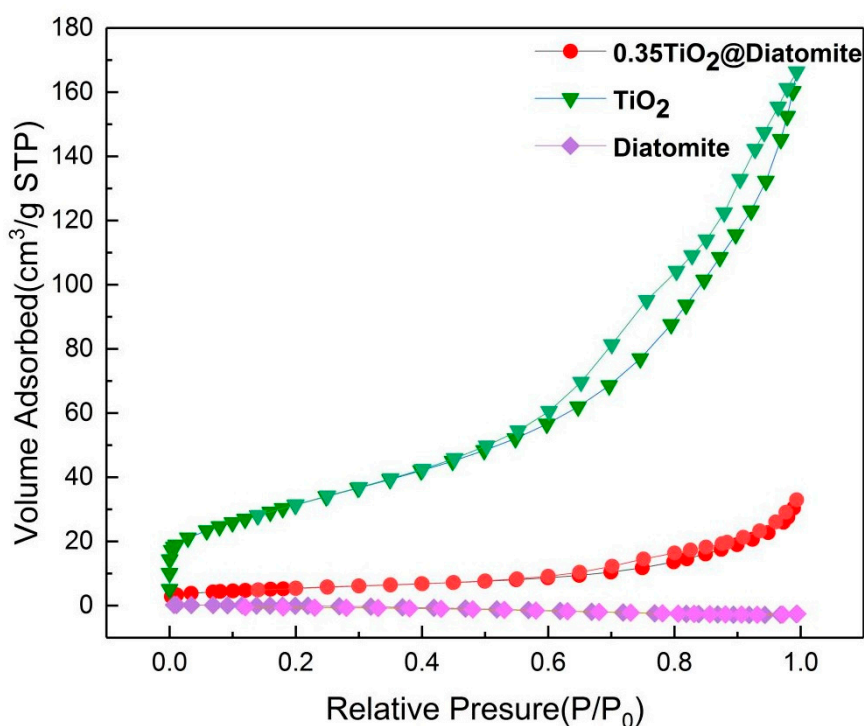


Figure 5. N₂ adsorption-desorption isotherms of diatomite, TiO₂, and 0.35TiO₂@diatomite.

2.5. Photoluminescence (PL) Spectra

For the photocatalysts, apart from the surface area, the nanoparticle size, and the light absorption range, the electron-hole recombination property is also significant. PL can be used to evaluate the electron-hole recombination property. In other words, fluorescence will occur when electron-hole recombination arises [48]. Therefore, the rate of electron-hole recombination is inversely proportional to the fluorescence intensity, and thus a lower fluorescence intensity represents a lower electron and hole recombination rate and a higher photocatalytic activity [49,50]. As shown in Figure 6, the PL of different catalysts was measured at an excitation wavelength of 300 nm. The strongest peaks of different catalysts all appear within approximately 400 nm; however, their emission intensity varies significantly. For photocatalytic reactions, reducing the electron-hole recombination rate is an important goal. In other words, a low electron-hole recombination rate is favorable for a photocatalytic reaction. Among the catalysts applied, 0.35TiO₂@diatomite has the lowest emission intensity, indicating that it has the lowest electron-hole recombination rate and thus possesses a better photocatalytic performance. The reduction of the luminescence intensity may be related to the Ti-O-Si band and ascribed to the increased electron capture centering on the surface of the TiO₂ nanoparticles, or an enhancement of the non-radiation-decay channels because of the SiO₂ around the TiO₂ nanoparticles.

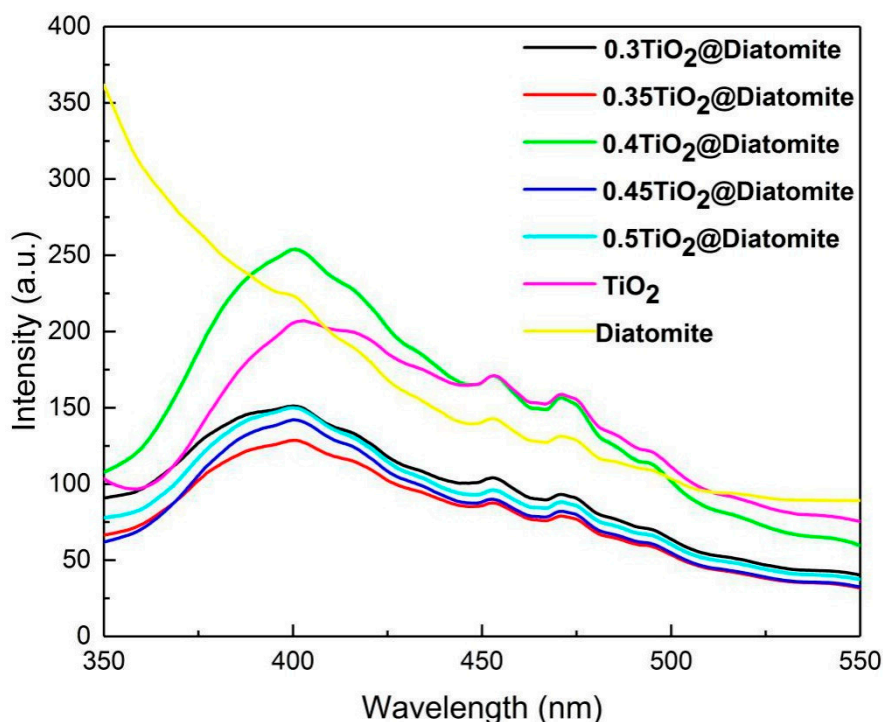


Figure 6. Photoluminescence (PL) spectra of TiO₂, diatomite, and XTiO₂@diatomite.

Therefore, it can be concluded that the photocatalytic performance of 0.35TiO₂@diatomite may be better than that of the other catalysts. This result is consistent with that obtained from the UV-vis diffuse reflectance spectra, confirming that 0.35TiO₂@diatomite is the optimal catalyst.

2.6. Photocatalytic Performance of Different Catalysts

The TiO₂ photocatalyst has a wide range of applications, such as air purification and sewage treatment. To evaluate the photocatalytic performance of different catalysts, a 5 W ultraviolet light source was used. Methylene blue (MB) was selected as the target pollutant to determine the optimal catalyst, and the optimal catalyst was then selected as the degradation catalyst for gaseous organic pollutants, such as acetone, benzene, methanol, and ethanol. Compared with pure TiO₂, the XTiO₂@diatomite composite shows a relatively larger adsorption capacity for MB in spite of its

lower specific surface area and pore volume. As shown in Figure 8a, minor differences appeared in different catalysts. With the catalyst of $0.35\text{TiO}_2@\text{diatomite}$, the concentration of MB was nearly close to 0 within 90 min under UV light irradiation, and thus the degradation rate was faster than in the other similar photocatalysts. Clearly, $0.35\text{TiO}_2@\text{diatomite}$ (recorded as the optimal catalyst) showed the highest degradation rate for the photocatalytic degradation of MB. The MB degradation efficiency of pure diatomite is shown in Figure 8a, in which the concentration of MB remains almost unchanged as the irradiation time increases, indicating that the photocatalytic activity of $\text{TiO}_2@\text{diatomite}$ is weak in the absence of TiO_2 , and that the photocatalytic activity of $X\text{TiO}_2@\text{diatomite}$ is better than that of pure TiO_2 , suggesting a synergy effect between TiO_2 and diatomite (which may benefit from the formation of Si-O-Ti bonds). Because a Si-O-Ti bond can be formed when the surface of diatomite is covered with hydroxyl and silanol, this special structure allows TiO_2 to laboriously combine with diatomite, and further enhances its dispersibility, thereby significantly increasing its photocatalytic performance [46]. Among the types of $X\text{TiO}_2@\text{diatomite}$ applied, the photocatalytic activity of $0.35\text{TiO}_2@\text{diatomite}$ was better than that of the other catalysts. In addition, the photocatalytic activity of $\text{TiO}_2@\text{diatomite}$ is not simply promoted by the increasing load ratio of TiO_2 to diatomite. By contrast, excessive loading amounts of TiO_2 can in turn reduce the photocatalytic capability. This was confirmed through $0.35\text{TiO}_2@\text{diatomite}$, which exhibited the highest performance. This can be explained by the fact that excessive TiO_2 causes an agglomeration of TiO_2 on the surface of the diatomite, and thus reduces the photocatalytic performance of $\text{TiO}_2@\text{diatomite}$. This result agrees with the results obtained from the UV-vis diffuse reflectance spectra, PL spectra, and degree of aggregation shown on the SEM images. Therefore, $0.35\text{TiO}_2@\text{diatomite}$ was selected for the degradation experiment of the following gaseous organic pollutants.

Figure 8b,c show the degradation results of gaseous acetone and gaseous benzene, respectively. The gas concentration was controlled by adding 1 mL of saturated gas at room temperature to each of the six headspace bottles with three capacities (100, 200, and 500 mL), which were labeled as 100 mL(1), 100 mL(2), 200 mL(1), 200 mL(2), 500 mL(1), and 500 mL(2). In this experiment, bottles with the volumes shown in Figure 8c were used to degrade the gases, bottles of the same volume were used in repeated experiments three times, and the data were averaged to verify the accuracy. As can be seen from Figure 8b, under UV-Vis light irradiation, the optimal catalyst showed an excellent photocatalytic performance for gaseous acetone at different concentrations. In the experiment on the degradation of gaseous acetone, the concentration of gaseous acetone reached close to 0 in 90 min under UV-Vis light irradiation. This means that gaseous acetone can be completely decomposed in only 90 min at a fast rate, and slow decomposition can be completely achieved within 120 min. This is because the concentration of acetone is so high that it cannot be completely degraded within 90 min. In other words, after 90 min of irradiation, the degradation rate of $0.35\text{TiO}_2@\text{diatomite}$ for gaseous acetone reaches up to 100%, which is greater than in most other studies [51]. From Figure 8c, it can be seen that gaseous benzene is degraded within 90 min. However, most of the gaseous benzene with different concentrations cannot be completely degraded. One possible reason for this is that the structure of a benzene molecule is extremely stable and difficult to break. Another possible reason is that the concentration of gaseous benzene is too high to be completely degraded. In this study, only two gaseous organic pollutants were investigated. In the future, we will study the degradation of the catalyst under other gaseous organic pollutants (such as methanol, ethanol, propanol, formaldehyde, and acetaldehyde) and summarize whether the effects on the polar and non-polar organics are identical.

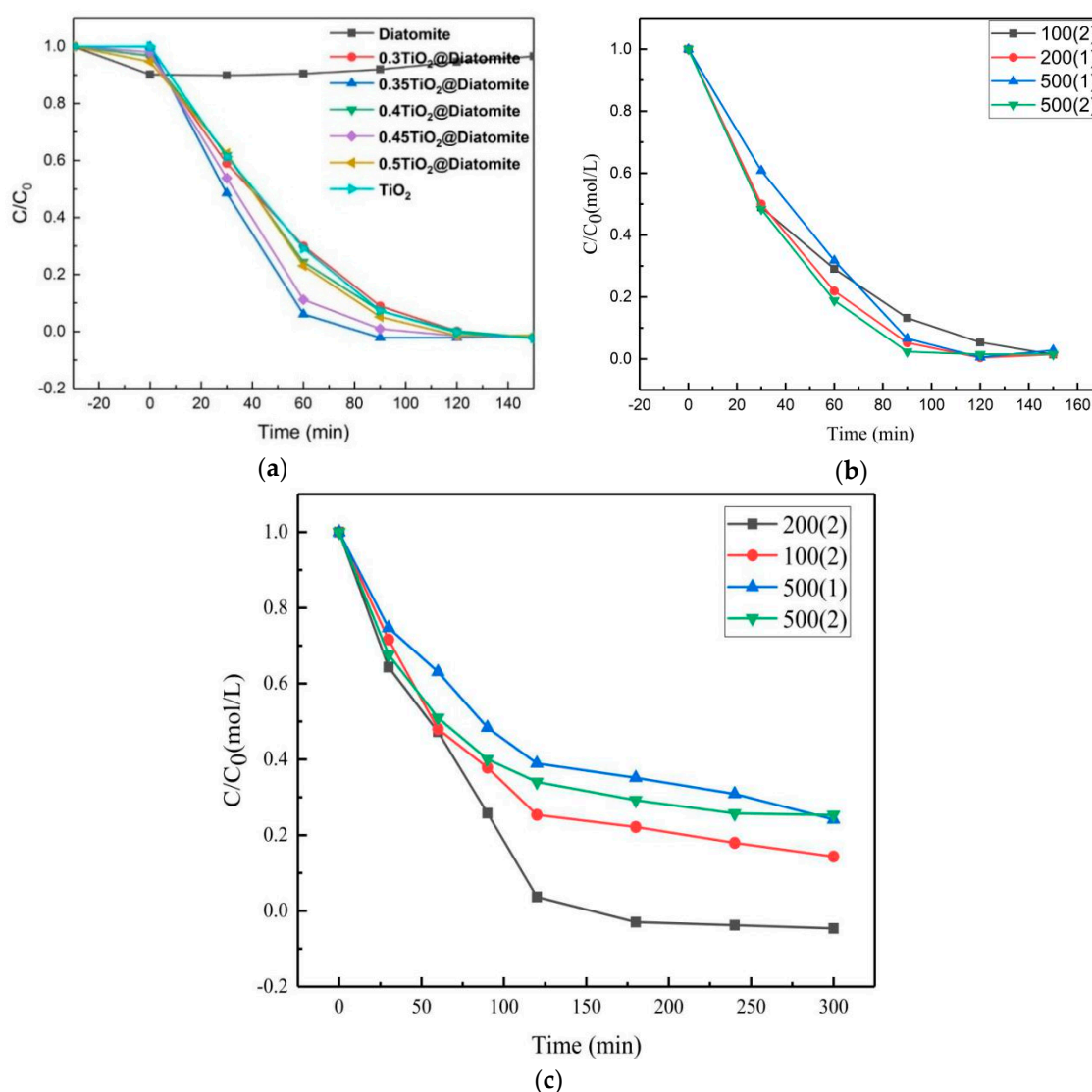


Figure 7. (a) Plots of the methylene blue (MB) photodegradation over various catalysts under UV irradiation. (b) Plots of the photodegradation of various concentrations of gaseous acetone over 0.35TiO_2 @diatomite under UV-Vis light irradiation. (c) Plots of the photodegradation of benzene at various concentrations over 0.35TiO_2 @diatomite under UV-Vis light irradiation.

3. Experimental Section

3.1. Chemicals and Materials

Diatomite (Macklin, Shanghai, China), titanium tetrachloride (TiCl_4 , analytical reagent, Adamas, Beijing, China), absolute ethanol (analytical reagent, Tianjin Damao Chemical Reagents Factory, Tianjin, China), benzene (analytical reagent, Tianjin Damao Chemical Reagents Factory, Tianjin, China), acetone (analytical reagent, Tianjin Damao Chemical Reagents Factory, Tianjin, China), and deionized water were used for the synthesis of TiO_2 and diatomite/ TiO_2 . During the process of synthesizing diatomite/ TiO_2 , the only difference from TiO_2 is that a certain amount of diatomite is added to the synthetic process for TiO_2 . All the reagents listed were used as purchased and without further treatment.

3.2. Catalyst Preparation

The TiO_2 @diatomite was prepared using a facile solvothermal method applying absolute ethanol as a solvent. Pure ethanol (50 mL) was transferred into a three-necked flask (250 mL) placed in an ice

bath and stirred for 30 min. Then, 0.5 mL of deionized water (0.5 mL) was added. After 5 min, TiCl_4 (2 mL) was added dropwise. The mixture was stirred until it became a transparent light-yellow solution. This solution was transferred to a dry Teflon-lined stainless-steel autoclave (100 mL) containing a certain amount of diatomite, and stirred evenly. The resulting mixture was then kept at $200\text{ }^\circ\text{C}$ for 12 h in an oven. After cooling to room temperature, the white precipitates were filtered off, and washed with ethanol and deionized water several times until the pH of the filtrate reached approximately 7. The chlorine was also removed through the washing process. The collected precipitates were dried at $80\text{ }^\circ\text{C}$ for 10 h in the oven to afford TiO_2 @diatomite. Detailed steps regarding the synthesis of TiO_2 @diatomite are also shown in Figure ?? . For convenience, the catalysts are denoted as XTiO_2 @diatomite, where X represents the mass ratio of TiO_2 to diatomite (because diatomite cannot be expressed in moles). The pure TiO_2 was prepared according to the above procedure, except with the addition of diatomite steps.

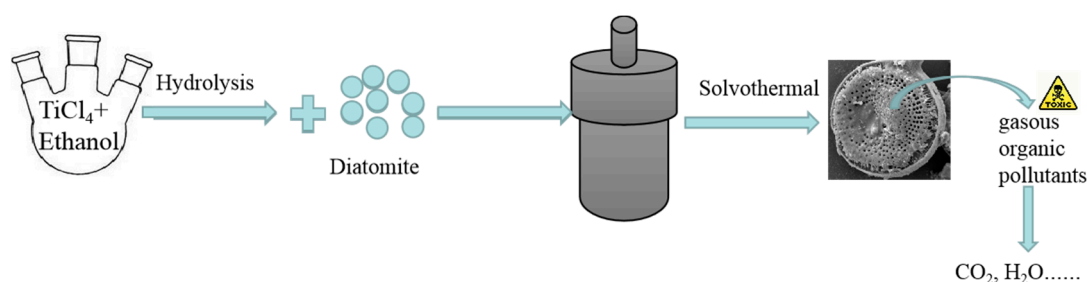


Figure 8. Synthesis procedure for XTiO_2 @diatomite catalysts.

3.3. Characterization

The catalysts were characterized based on X-ray diffraction patterns (XRD, Ultiam IV) recorded using $\text{Cu K}\alpha$ radiation at a scan rate of $5^\circ/\text{min}$. Their microstructures were observed using field-emission SEM (JEOL-JSM-7800F (Tokyo, Japan) with an energy dispersive spectrometer and S-4700 at an acceleration voltage of 20 KV), TEM (Hitachi-HT7700 (Tokyo, Japan) at an acceleration voltage of 120 KV and JEM-ARM-200F), and HRTEM (JEOL, JEM-ARM200F, Tokyo, Japan). The specific surface area and pore size distribution of the different catalysts were determined using a Brunauer–Emmett–Teller (BET) instrument with nitrogen adsorption at 77 K (Micrometrics ASAP 2020, Georgia, USA). In addition, the ultraviolet-visible spectrophotometer (Shimadzu UV-3600, Tokyo, Japan) was used to analyze the UV-vis diffuse reflectance spectra of the prepared catalysts. Moreover, the electron hole recombination rate was measured using a photoluminescence spectrometer (FL-7000, Hitachi, Tokyo, Japan) to evaluate the photocatalytic activity.

3.4. Evaluation of Photocatalytic Activity

The photocatalytic activities of different catalysts were initially evaluated based on the degradation of MB under UV-light irradiation at ambient temperature [52]. During this process, the catalyst (0.05 g) was dispersed in an MB solution (10 of MB (50 mg/mL, 30 mL)) in a Petri dish. A portion of MB solution was taken every 30 min for measurements using an ultraviolet-visible spectrophotometer. The degradation rate was determined by monitoring the change in concentration of the MB over time using an ultraviolet-visible spectrophotometer (Shimadzu UV-3600). The catalyst with the highest degradation rate was chosen for degradation of the different gaseous organic pollutants, including acetone and benzene. These degradation processes were carried out in sealed headspace bottles with different volumes (100, 200, and 500 mL). The concentration of gas was controlled by adding equal volumes of saturated gas to different volumes of sealed headspace bottles (to the best of our knowledge, at the same temperature, the concentration of saturated gas is constant). The specific experimental details are similar to those of the process of MB degradation described above [52], except that the MB solution was replaced with gaseous phase organic pollutants. The details of the experiment are as follows: A catalyst (0.05 g) was added to each of the headspace bottles, and 1 mL of saturated gaseous

phase pollutants at room temperature was transferred to the sealed headspace bottles using a gas chromatography syringe with a capacity of 2.5 mL. In addition, the initial concentrations of gaseous acetone and benzene in the 100, 200, and 500 mL headspace bottles were approximately 2.95×10^{-3} , 1.63×10^{-3} , and 6.85×10^{-4} mol/L, respectively. A xenon lamp (30 W) was adopted as a light source during the photocatalytic degradation process. The headspace bottle was placed under the light, and the bottle was directly irradiated. The whole process was degraded at room temperature. Throughout the degradation process, no heating and any agitation were used. Simultaneously, gases were taken every 30 min and the corresponding concentrations of organic gaseous pollutants were determined using gas chromatography-mass spectrometry (GC-MS). In addition, the degradation reaction of the organic gaseous pollutants was kept at ambient temperature. Four sealed headspace bottles of each gas were used for gaseous pollutant degradation. All reactions were repeated three times in parallel.

4. Conclusions

In conclusion, we successfully prepared a series of TiO₂@diatomite catalysts using a facile solvothermal method applying anhydrous ethanol as a solvent for the removal of VOCs. The XRD patterns showed that TiO₂ in the catalyst is in an anatase phase, and the introduction of diatomite has no effect on the crystal structure of TiO₂. SEM and TEM images indicated that the size of the TiO₂ nanoparticles is approximately 10–15 nm, and the morphologies of most of the TiO₂ nanoparticles are square-like. In addition, for the TiO₂@diatomite, the TiO₂ nanoparticles are uniformly immobilized on the diatomite. Based on photocatalytic activity tests, 0.35TiO₂@diatomite (with a TiO₂ to diatomite mass ratio of 0.35) displayed higher photocatalytic activity compared with that at other ratios, pure TiO₂, and pure diatomite. This result is consistent with the characterization results of the UV-vis diffuse reflectance spectra and PL spectra. The photocatalytic performance and GC-MS test results showed that 0.35TiO₂@diatomite can be used to effectively remove acetone and benzene. In addition, both TiO₂ and diatomite are low-cost, non-toxic, harmless, and stable. Therefore, a TiO₂@diatomite catalyst could potentially be applied in the area of building construction and interior decoration.

Author Contributions: Conceptualization, X.L. & J.Y.; Methodology, X.L.; Software, X.L.; & Q.Y. & B.Y.; Formal Analysis, X.L.; Data curation, X.L. & J.Y.; Writing-Original draft preparation, X.L.; Writing-Review & Editing, X.L. & J.Y.; Visualization, X.L. & J.Y. & Y.H.; Supervision, J.Y.; Funding acquisition, J.Y. All authors have read and agreed to the published version of the manuscript.

Funding: This research received no external funding.

Acknowledgments: The authors express their gratitude to the Analysis and Test Center of Beijing University of Chemical Technology for the received help.

Conflicts of Interest: The authors declare no conflict of interest.

References

1. Knudsen, H.N.; Kjaer, U.D.; Nielsen, P.A.; Wolkoff, P. Sensory and chemical characterization of voc emissions from building products: Impact of concentration and air velocity. *Atmos. Environ.* **1999**, *33*, 1217–1230. [[CrossRef](#)]
2. Salthammer, T. Emission of volatile organic compounds from furniture coatings. *Indoor Air* **1996**, *7*, 189–197. [[CrossRef](#)]
3. Wolkoff, P. Volatile organic compounds sources, measurements, emissions, and the impact on indoor air quality. *Indoor Air* **1995**, *5*, 5–73. [[CrossRef](#)]
4. Meininghaus, R.; Gunnarsen, L.; Knudsen, H.N. Diffusion and sorption of volatile organic compounds in building materials—Impact on indoor air quality. *Environ. Sci. Technol.* **2000**, *34*, 3101–3108. [[CrossRef](#)]
5. Dai, H.; Jing, S.; Wang, H. VOC characteristics and inhalation health risks in newly renovated residences in Shanghai, China. *Sci. Total Environ.* **2017**, *577*, 73–83. [[CrossRef](#)]
6. Bentayeb, M.; Simoni, M.; Norback, D.; Baldacci, S.; Maio, S.; Viegi, G.; Annesi-Maesano, I. Indoor air pollution and respiratory health in the elderly. *J. Environ. Sci. Health A* **2013**, *48*, 1783–1789. [[CrossRef](#)]

7. Ye, D.; Klein, M.; Chang, H.H.; Sarnat, J.A.; Mulholland, J.A.; Edgerton, E.S.; Winkler, A.; Tolbert, P.E.; Sarnat, S.E. Estimating acute cardiorespiratory effects of ambient volatile organic compounds. *Epidemiology (Camb. Mass.)* **2017**, *28*, 197. [[CrossRef](#)]
8. World Health Organization. *Burden of Disease from the Joint Effects of Household and Ambient Air Pollution for 2016; Social and Environmental Determinants of Health Department*: Geneva, Switzerland, 7 November 2018.
9. Lam, R.C.W.; Leung, M.K.H.; Leung, D.Y.C.; Vrijmoed, L.L.P.; Yam, W.C.; Ng, S.P. Visible-light-assisted photocatalytic degradation of gaseous formaldehyde by parallel-plate reactor coated with Cr ion-implanted TiO₂ thin film. *Sol. Energy. Mat. Sol. C.* **2007**, *91*, 54–61. [[CrossRef](#)]
10. Jeong, J.; Sekiguchi, K.; Sakamoto, K. Photochemical and photocatalytic degradation of gaseous toluene using short-wavelength uv irradiation with TiO₂ catalyst: Comparison of three uv sources. *Chemosphere* **2004**, *57*, 663–671. [[CrossRef](#)]
11. Higashimoto, S.; Tanihata, W.; Nakagawa, Y.; Azuma, M.; Ohue, H.; Sakata, Y. Effective photocatalytic decomposition of voc under visible-light irradiation on n-doped TiO₂ modified by vanadium species. *Appl. Catal. A Gen.* **2008**, *340*, 98–104. [[CrossRef](#)]
12. Azzouz, I.; Habba, Y.G.; Capochichi-Gnambodoe, M.; Marty, F.; Vial, J.; Leprince-Wang, Y.; Bourouina, T. Zinc oxide nano-enabled microfluidic reactor for water purification and its applicability to volatile organic compounds. *Microsyst. Nanoeng.* **2018**, *4*, 1–7. [[CrossRef](#)]
13. Ghorbani Shahna, F.; Bahrami, A.; Ebrahimi, H. The hybrid effect of non-thermal plasma and activated carbon-zinc oxide nanocomposite on the removal of volatile organic compounds in air. *Iran Occup. Health* **2017**, *14*, 24–13.
14. Meng, F.; Zheng, H.; Chang, Y.; Zhao, Y.; Li, M.; Wang, C.; Sun, Y.; Liu, J. One-step synthesis of Au/SnO₂/RGO nanocomposites and their VOC sensing properties. *IEEE. Trans. Nanotechnol.* **2018**, *17*, 212–219. [[CrossRef](#)]
15. Kaur, M.; Kumar, A.G. Synthesis and Characterization of Mesoporous SnO₂ Photocatalyst for Degradation of Dye and Volatile Organic Compound. Ph.D. Thesis, 2016.
16. Wang, L.; Xu, X.; Wang, Y.; Wang, X.; Shi, F.-N. Sulfur vacancy-rich CdS loaded on filter paper-derived 3D nitrogen-doped mesoporous carbon carrier for photocatalytic VOC removal. *Inorg. Chem. Front.* **2018**, *5*, 1470–1476. [[CrossRef](#)]
17. Zhou, H.; Wen, Z.; Liu, J.; Ke, J.; Duan, X.; Wang, S. Z-scheme plasmonic Ag decorated WO₃/Bi₂WO₆ hybrids for enhanced photocatalytic abatement of chlorinated-VOCs under solar light irradiation. *Appl. Catal. B Environ.* **2019**, *242*, 76–84. [[CrossRef](#)]
18. Šuligoj, A.; Štangar, U.L.; Ristić, A.; Mazaj, M.; Verhovšek, D.; Tušar, N.N. TiO₂–SiO₂ films from organic-free colloidal TiO₂ anatase nanoparticles as photocatalyst for removal of volatile organic compounds from indoor air. *Appl. Catal. B Environ.* **2016**, *184*, 119–131. [[CrossRef](#)]
19. Weon, S.; Choi, E.; Kim, H.; Kim, J.Y.; Park, H.J.; Kim, S.M.; Kim, W.; Choi, W. Active {001} facet exposed TiO₂ nanotubes photocatalyst filter for volatile organic compounds removal: From material development to commercial indoor air cleaner application. *Environ. Sci. Technol.* **2018**, *52*, 9330–9340. [[CrossRef](#)]
20. Haghghatmamaghani, A.; Haghghat, F.; Lee, C.S. Performance of various commercial TiO₂ in photocatalytic degradation of a mixture of indoor air pollutants: Effect of photocatalyst and operating parameters. *Sci. Technol. Built. Environ.* **2019**, *25*, 600–614. [[CrossRef](#)]
21. Li, F.B.; Li, X.Z.; Ao, C.H.; Lee, S.C.; Hou, M.F. Enhanced photocatalytic degradation of VOCs using Ln³⁺–TiO₂ catalysts for indoor air purification. *Chemosphere* **2005**, *59*, 787–800. [[CrossRef](#)]
22. Tidahy, H.L.; Siffert, S.; Lamonier, J.F.; Zhilinskaya, E.A.; Aboukais, A.; Yuan, Z.-Y.; Vantomme, A.; Su, B.-L.; Canet, X.; De Weireld, G.; et al. New Pd/hierarchical macro-mesoporous ZrO₂, TiO₂ and ZrO₂-TiO₂ catalysts for VOCs total oxidation. *Appl. Catal. A Gen.* **2006**, *310*, 61–69. [[CrossRef](#)]
23. Pham, T.D.; Lee, B.K. Selective removal of polar VOCs by novel photocatalytic activity of metals co-doped TiO₂/PU under visible light. *Chem. Eng. J.* **2017**, *307*, 63–73. [[CrossRef](#)]
24. Ochiai, T.; Tago, S.; Hayashi, M.; Tawarayama, H.; Hosoya, T.; Fujishima, A. TiO₂-impregnated porous silica tube and its application for compact air-and water-purification units. *Catalysts* **2015**, *5*, 1498–1506. [[CrossRef](#)]
25. Shayegan, Z.; Lee, C.S.; Haghghat, F. TiO₂ photocatalyst for removal of volatile organic compounds in gas phase—A review. *Chem. Eng. J.* **2018**, *334*, 2408–2439. [[CrossRef](#)]
26. Ji, J.; Xu, Y.; Huang, H.; He, M.; Liu, S.; Liu, G.; Xie, R.; Feng, Q.; Shu, Y.; Zhan, Y. Mesoporous TiO₂ under VUV irradiation: Enhanced photocatalytic oxidation for VOCs degradation at room temperature. *Chem. Eng. J.* **2017**, *327*, 490–499. [[CrossRef](#)]

27. Ao, C.H.; Lee, S.C.; Mak, C.L.; Chan, L.Y. Photodegradation of volatile organic compounds (VOCs) and NO for indoor air purification using TiO₂: Promotion versus inhibition effect of NO. *Appl. Catal. B Environ.* **2003**, *42*, 119–129. [[CrossRef](#)]
28. Hwang, J.Y.; Kim, H.M.; Lee, S.K. High-Energy, High-Rate, Lithium–Sulfur Batteries: Synergetic Effect of Hollow TiO₂-Webbed Carbon Nanotubes and a Dual Functional Carbon-Paper Interlayer. *Adv. Energy Mater.* **2016**, *6*, 1501480. [[CrossRef](#)]
29. Zhu, S.R.; Wu, M.K.; Zhao, W.N.; Yi, F.Y.; Tao, K.; Han, L. Fabrication of heterostructured BiOBr/Bi₂₄O₃1Br10/TiO₂ photocatalyst by pyrolysis of MOF composite for dye degradation. *J. Solid State Chem.* **2017**, *255*, 17–26. [[CrossRef](#)]
30. Yan, L.; Gu, Y.; Han, L.; Wang, P.; Li, H.; Yan, T.; Kuboon, S.; Shi, L.; Zhang, D. Dual Promotional Effects of TiO₂-Decorated Acid-Treated MnO_x Octahedral Molecular Sieve Catalysts for Alkali-Resistant Reduction of NO_x. *ACS Appl. Mater. Interfaces* **2019**, *11*, 11507–11517. [[CrossRef](#)]
31. Li, M.; Lu, B.; Ke, Q.F.; Guo, Y.J.; Guo, Y.P. Synergetic effect between adsorption and photodegradation on nanostructured TiO₂/activated carbon fiber felt porous composites for toluene removal. *J. Hazard. Mater.* **2017**, *333*, 88–98. [[CrossRef](#)]
32. Zuo, R.; Du, G.; Zhang, W.; Liu, L.; Liu, Y.; Mei, L. Photocatalytic degradation of methylene blue using TiO₂ impregnated diatomite. *Adv. Mater. Sci. Eng.* **2014**, *2014*, 170148. [[CrossRef](#)]
33. PENNY Crossley. Clarifying matters-world diatomite reviewed. *Ind. Miner.* **2000**, *390*, 119–141.
34. Al-Degs, Y.; Khraisheh, M.A.M.; Tutunji, M.F. Sorption of Lead Ions on Diatomite and Manganese Oxides Modified Diatomite. *Water Res.* **2001**, *35*, 3724–3728. [[CrossRef](#)]
35. Khraisheh, M.A.M.; Al-degs, Y.S.; Mcminn, W.A.M. Remediation of wastewater containing heavy metals using raw and modified diatomite. *Chem. Eng. J.* **2004**, *99*, 177–184. [[CrossRef](#)]
36. Niu, L.; Xian, G.; Long, Z.; Zhang, G.; Zhou, N. MnCeO_x/diatomite catalyst for persulfate activation to degrade organic pollutants. *J. Environ. Sci.* **2020**, *89*, 206–217. [[CrossRef](#)]
37. He, H.; Luo, Z.; Yu, C. Diatomite-anchored g-C₃N₄ nanosheets for selective removal of organic dyes. *J. Alloys Compd.* **2020**, *816*, 152652. [[CrossRef](#)]
38. Gao, R.; Sun, Q.; Fang, Z.; Li, G.T.; Jia, M.; Hou, X. Preparation of nano-TiO₂/diatomite-based porous ceramics and their photocatalytic kinetics for formaldehyde degradation. *Int. J. Miner. Metall. Mater.* **2018**, *25*, 73–79. [[CrossRef](#)]
39. Wu, Z.; Zhu, Z.; Hao, X.; Zhou, W.; Han, J.; Tang, X.; Yao, S.; Zhang, X. Enhanced oxidation of naphthalene using plasma activation of TiO₂/diatomite catalyst. *J. Hazard. Mater.* **2018**, *347*, 48–57. [[CrossRef](#)]
40. Chen, Y.; Liu, K. Preparation of granulated N-doped TiO₂/diatomite composite and its applications of visible light degradation and disinfection. *Powder Technol.* **2016**, *303*, 176–191. [[CrossRef](#)]
41. Ao, M.; Liu, K.; Tang, X.; Li, Z.; Peng, Q.; Huang, J. BiOCl/TiO₂/diatomite composites with enhanced visible-light photocatalytic activity for the degradation of rhodamine B. *Beilstein. J. Nanotech.* **2019**, *10*, 1412–1422. [[CrossRef](#)]
42. Xu, H.; Reunchan, P.; Ouyang, S.; Tong, H.; Umezawa, N.; Kako, T.; Ye, J. Anatase TiO₂ single crystals exposed with high-reactive {111} facets toward efficient H₂ evolution. *Chem. Mater.* **2013**, *25*, 405–411. [[CrossRef](#)]
43. Roy, N.; Park, Y.; Sohn, Y. Green synthesis of anatase TiO₂ nanocrystals with diverse shapes and their exposed facets-dependent photoredox activity. *ACS Appl. Mater. Interfaces* **2014**, *6*, 16498–16507. [[CrossRef](#)]
44. Sun, Z.; Yang, X.; Zhang, G.; Zheng, S.; Frost, R. A novel method for purification of low grade diatomite powders in centrifugal fields. *Int. J. Miner. Process.* **2013**, *125*, 18–26. [[CrossRef](#)]
45. Liu, E.; Kang, L.; Wu, F.; Sun, T.; Hu, X.; Yang, Y.; Liu, H.; Fan, J. Photocatalytic Reduction of CO₂ into Methanol over Ag/TiO₂ Nanocomposites Enhanced by Surface Plasmon Resonance. *Plasmonics* **2014**, *9*, 61–70. [[CrossRef](#)]
46. Wu, L.; Zhou, Y.; Nie, W.; Song, L.; Chen, P. Synthesis of highly monodispersed teardrop-shaped core-shell SiO₂/TiO₂ nanoparticles and their photocatalytic activities. *Appl. Surf. Sci.* **2015**, *351*, 320–326. [[CrossRef](#)]
47. Thommes, M.; Kaneko, K.; Neimark, A.V. Physisorption of gases, with special reference to the evaluation of surface area and pore size distribution (IUPAC Technical Report). *Pure Appl. Chem.* **2015**, *87*, 1051–1069. [[CrossRef](#)]
48. Yu, X.; Zhao, Z.; Zhang, J. One-step synthesis of ultrathin nanobelts-assembled urchin-like anatase TiO₂ nanostructures for highly efficient photocatalysis. *CrystEngComm* **2017**, *19*, 129–136. [[CrossRef](#)]

49. Xu, H.Q.; Hu, J.; Wang, D.; Li, Z.; Zhang, Q.; Luo, Y.; Yu, S.H.; Jiang, H.L. Visible-light photoreduction of CO₂ in a metal–organic framework: Boosting electron–hole separation via electron trap states. *J. Am. Chem. Soc.* **2015**, *137*, 13440–13443. [[CrossRef](#)]
50. Kang, Y.; Yang, Y.; Yin, L.C. Selective breaking of hydrogen bonds of layered carbon nitride for visible light photocatalysis. *Adv. Mater.* **2016**, *28*, 6471–6477. [[CrossRef](#)]
51. Choi, W.; Ko, J.Y.; Park, H.; Chung, J.S. Investigation on TiO₂-coated optical fibers for gas-phase photocatalytic oxidation of acetone. *Appl. Catal. B Environ.* **2001**, *31*, 209–220. [[CrossRef](#)]
52. Liu, S.; Yu, J.; Jaroniec, M. Tunable photocatalytic selectivity of hollow TiO₂ microspheres composed of anatase polyhedra with exposed {001} facets. *J. Am. Chem. Soc.* **2010**, *132*, 11914–11916. [[CrossRef](#)]



© 2020 by the authors. Licensee MDPI, Basel, Switzerland. This article is an open access article distributed under the terms and conditions of the Creative Commons Attribution (CC BY) license (<http://creativecommons.org/licenses/by/4.0/>).